



Non-destructive visualization of short circuits in lithium-ion batteries by a magnetic field imaging system

Suzuki, Shogo ; Okada, Hideaki ; Yabumoto, Kai ; Matsuda, Seiju ; Mima, Yuki ; Kimura, Noriaki ; Kimura, Kenjiro

(Citation)

Japanese Journal of Applied Physics, 60(5):056502

(Issue Date)

2021-05-01

(Resource Type)

journal article

(Version)

Version of Record

(Rights)

© 2021 The Japan Society of Applied Physics.

Content from this work may be used under the terms of the Creative Commons Attribution 4.0 license. Any further distribution of this work must maintain attribution to the author(s) and the title of the work, journal citation and DOI.

(URL)

<https://hdl.handle.net/20.500.14094/90008769>



REGULAR PAPER • OPEN ACCESS

Non-destructive visualization of short circuits in lithium-ion batteries by a magnetic field imaging system

To cite this article: Shogo Suzuki *et al* 2021 *Jpn. J. Appl. Phys.* **60** 056502

View the [article online](#) for updates and enhancements.

You may also like

- [Morphological Structure Characterizations in Lithium-Ion Battery \(LIB\) Slurry under Shear Rotational Conditions by On-Line Dynamic Electrochemical Impedance Spectroscopy \(EIS\) Method](#)
Zhilong Wang, Tong Zhao and Masahiro Takei
- [Analysis of a Phase Change Material for Thermal Management of a Lithium-Ion Battery](#)
Seyed Saeed Madani
- [A review on prognostics approaches for remaining useful life of lithium-ion battery](#)
C Su and H J Chen



Non-destructive visualization of short circuits in lithium-ion batteries by a magnetic field imaging system

Shogo Suzuki¹, Hideaki Okada¹, Kai Yabumoto¹, Seiju Matsuda¹, Yuki Mima^{2,3}, Noriaki Kimura^{2,3}, and Kenjiro Kimura^{1,3*}

¹Kobe University, 1-1, Rokkodai-cho, Nada-ku, Kobe-shi, Hyogo, 657-8501, Japan

²Integral Geometry Science, 1-5-6, Minatojima-minamimachi, Chuo-ku, Kobe-shi, Hyogo 650-0047, Japan

³NEDO, 1310, Omiya-cho, Saiwai-ku, Kawasaki-shi, Kanagawa, 212-0014, Japan

*E-mail: kimura@gold.kobe-u.ac.jp

Received December 3, 2020; revised March 27, 2021; accepted April 2, 2021; published online April 21, 2021

To develop a high-density and long-life lithium-ion battery, a technology is needed that allows non-destructive visualization of the spatial distribution of deteriorated parts after cycle test. In the present study, we measured the distribution of the magnetic field leaking from the lithium-ion battery during its operation. Based on the measurement results, we evaluated the spatial distribution of electric current density that corresponds to the reaction rate of the active material and the ion diffusion rate in the electrolyte solution inside a battery using the electric current reconstruction process. With respect to the changes in the internal state of the lithium-ion battery associated with cycle deterioration, we successfully visualized the part where the electrical conductivity has changed that is the deteriorated part causing the battery capacity to decrease inside the lithium-ion battery. © 2021 The Japan Society of Applied Physics

1. Introduction

Because of their high energy density and long life, lithium-ion batteries are widely used in electric vehicles, hybrid electric vehicles, mobile phones, etc. Lithium-ion batteries, however, are also known for forming dendritic lithium crystals, which deposit on negative electrodes during charging.^{1–4} Dendrites degrade the performance of the negative electrode and cause capacity deterioration.^{5–8} In addition, it has been reported that some overgrown dendrites penetrate separators, which causes short circuits that results in serious accidents such as ignition and burning of the organic solvent.^{9–12} Observation of the negative electrode cross-section using synchrotron hard X-ray microtomography¹ and microscopic observation of specially shaped cells^{13–15} demonstrated that the dendrites form due to the heterogeneous reactivity of the negative electrode. Accordingly, for a purpose of developing high-quality lithium-ion batteries, it is indispensable to establish a method for directly observing the phenomena occurring inside lithium-ion batteries to visualize the spatial non-uniformity of the reaction kinetics.^{16–19}

The methods for observing the non-uniformity of reactions include three-dimensional structural analysis using X-ray tomography,^{20,21} visualization of the lithium ions distribution using X-ray Absorption Spectroscopy,^{22–24} energy dispersive X-ray spectroscopy for element mapping,^{25,26} and the Raman spectroscopy to visualize the crystal structure distribution of active materials in lithium-ion batteries.^{27,28} Also, in this study, in contrast to the mentioned methods, by using a magnetic sensor we measured the distribution of magnetic field generated by the currents during operation of a lithium-ion battery. Then, based on these results, we developed a method to visualize the conductivity distribution inside a lithium-ion battery using the analytical relation between the solution of the current in a battery and the magnetic field it induces. Therefore, this paper deals with a non-destructive visualization of changes in conductivity

inside the lithium-ion battery associated with its cycle deterioration.

2. Experimental methods

Assigning the boundary conditions as the two-dimensional Fourier transform $f_x(k_x, k_y)$ and $f_y(k_x, k_y)$ of the measured magnetic field distribution in Eqs. (1) and (2), the analytical solution of the basic equation of the static magnetic field in free space without a magnetic source can be derived by Eqs. (3) and (4).²⁹ As shown in Fig. 1, the x -axis and y -axis are in the electrode plane direction. With the magnetic field reconstruction method using this solution, the magnetic field distribution on the surface of the lithium-ion battery can be obtained based on the measurements.

$$f_x(k_x, k_y) = \int_{-\infty}^{\infty} \int_{-\infty}^{\infty} e^{-ik_x x - ik_y y} H_x(x, y, 0) dx dy \quad (1)$$

$$f_y(k_x, k_y) = \int_{-\infty}^{\infty} \int_{-\infty}^{\infty} e^{-ik_x x - ik_y y} H_y(x, y, 0) dx dy \quad (2)$$

$$\begin{aligned} H_x(x, y, z_0) &= \frac{1}{(2\pi)^2} \int_{-\infty}^{\infty} \int_{-\infty}^{\infty} e^{ik_x x + ik_y y} f_x(k_x, k_y) e^{\sqrt{k_x^2 + k_y^2} z_0} dk_x dk_y \\ &\quad (3) \end{aligned}$$

$$\begin{aligned} H_y(x, y, z_0) &= \frac{1}{(2\pi)^2} \int_{-\infty}^{\infty} \int_{-\infty}^{\infty} e^{ik_x x + ik_y y} f_y(k_x, k_y) e^{\sqrt{k_x^2 + k_y^2} z_0} dk_x dk_y \\ &\quad (4) \end{aligned}$$

Further, the relationship between the magnetic field distribution on the battery surface (Fig. 1) and conductivity inside the battery can be derived in the following manner. In the Eq. (5), as shown in Fig. 1, h_T is the distance between the electrodes, h is the thickness of the electrode and $\sigma(x, y)$ is the conductivity distribution between the electrodes of a



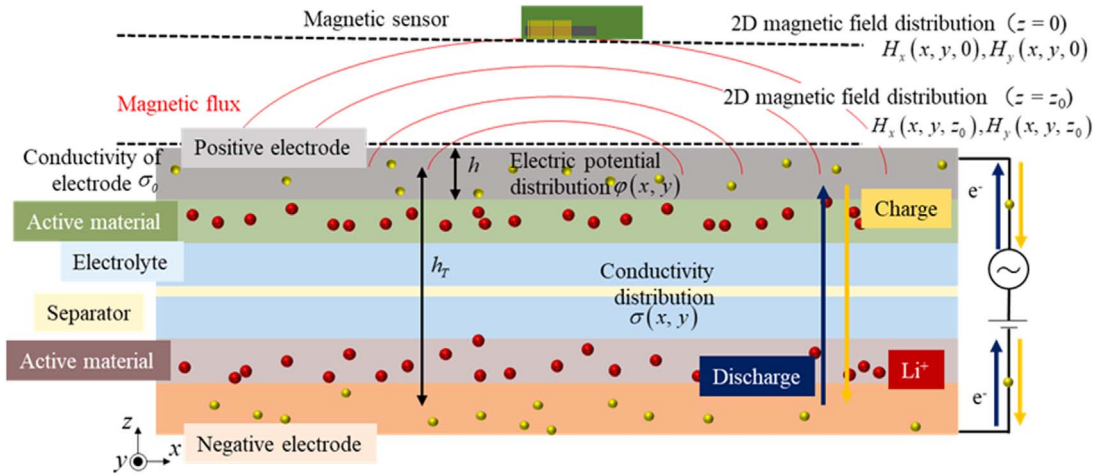


Fig. 1. (Color online) Schematic diagram for measuring the magnetic field during the operation of a lithium-ion battery.

lithium-ion battery, $\varphi(x, y)$ is the two-dimensional potential distribution on the electrode surface, z_0 is the electrode coordinate and σ_0 is the electrode conductivity.

30 pT/Hz^{0.5} at 1 Hz) that was developed based on the magneto-impedance effect.³¹⁾ The magnetic field distribution was measured by controlling the X and Y stepping motors and

$$\Delta H(x, y, z) = \begin{bmatrix} h_T^{-1} h \frac{\partial}{\partial y} (\sigma(x, y) \varphi(x, y)) \delta(z - z_0) - \sigma_0 h \frac{\partial \varphi(x, y)}{\partial y} \delta'(z - z_0) \\ h_T^{-1} h \frac{\partial}{\partial x} (\sigma(x, y) \varphi(x, y)) \delta(z - z_0) - \sigma_0 h \frac{\partial \varphi(x, y)}{\partial x} \delta'(z - z_0) \\ 0 \end{bmatrix}. \quad (5)$$

$Q_x(k_x, k_y, z_0)$ and $Q_y(k_x, k_y, z_0)$ are two-dimensional Fourier transforms of the x and y components of the magnetic field on the battery surface according to Eqs. (6) and (7).

$$Q_x(k_x, k_y, z_0) = \int_{-\infty}^{\infty} \int_{-\infty}^{\infty} e^{-ik_x x - ik_y y} H_x(x, y, z_0) dx dy \quad (6)$$

$$Q_y(k_x, k_y, z_0) = \int_{-\infty}^{\infty} \int_{-\infty}^{\infty} e^{-ik_x x - ik_y y} H_y(x, y, z_0) dx dy. \quad (7)$$

Using Eqs. (6) and (7), $\varphi(x, y)$ can be derived from Eq. (5) as shown in Eq. (8).³⁰⁾ Furthermore, the analytical solution $\sigma(x, y)$ of the two-dimensional conductivity distribution in the battery can be obtained from Eq. (9). This distribution represents the electric current between the electrodes, and corresponds to the reaction rate of the active material and the ion diffusion rate in the electrolyte solution. From the magnetic field distribution on the surface determined by this method, the conductivity distribution inside the battery can be reconstructed

$$\varphi(x, y) = \frac{1}{(2\pi)^2} \int_{-\infty}^{\infty} \int_{-\infty}^{\infty} e^{ik_x x + ik_y y} \frac{2\{ik_y Q_x(k_x, k_y, z_0) - ik_x Q_y(k_x, k_y, z_0)\}}{h\sigma_0(k_x^2 + k_y^2)(h\sqrt{k_x^2 + k_y^2} - 1)} dk_x dk_y \quad (8)$$

$$\sigma(x, y) = h h_T \sigma_0 \frac{\left(\frac{\partial^2}{\partial x^2} + \frac{\partial^2}{\partial y^2}\right) \varphi(x, y)}{\varphi(x, y)}. \quad (9)$$

Figure 2 shows a schematic diagram of the magnetic imaging system. We used a magnetic sensor (Detectability:

performing two-dimensional scanning. Further, the angle of the magnetic sensor was adjusted by the θ stepping motor to measure the x component H_x and the y component H_y of the magnetic field. When applying the alternating current with the 1 Hz frequency source to the battery, the generated magnetic field was detected by the magnetic sensor. After digitalization of the magnetic sensor signals by a 16 bit A/D converter, magnetic field phase delay was determined compared to the reference signal of the current source. Then, the conductivity distribution in the lithium-ion battery was reconstructed following Eqs. (4) and (9).

3. Results and discussion

In the cycle test, we used a laminated single-layer lithium-ion battery having an electrode size of 80 mm × 240 mm. The cathode consisted of NMC622 (NMC: Nickel-Manganese-Cobalt cathode) active material, acetylene black (AB) as a conductive additive, and polyvinylidene fluoride (PVDF) at the ratio of 94:3:3. The anode consisted of graphite as active

material, AB, carboxymethylcellulose (CMC) as a thickener, and styrene-butadiene rubber (SBR) as a binder at the ratio of 98.5:0.5:1:1. The electrolyte was 1.0 M lithium hexafluorophosphate (LiPF₆) solution in ethylene carbonate (EC)/dimethyl carbonate (DMC)/ethyl methyl carbonate (EMC) at the ratio of 1/1/1, with 1% doping with vinylene

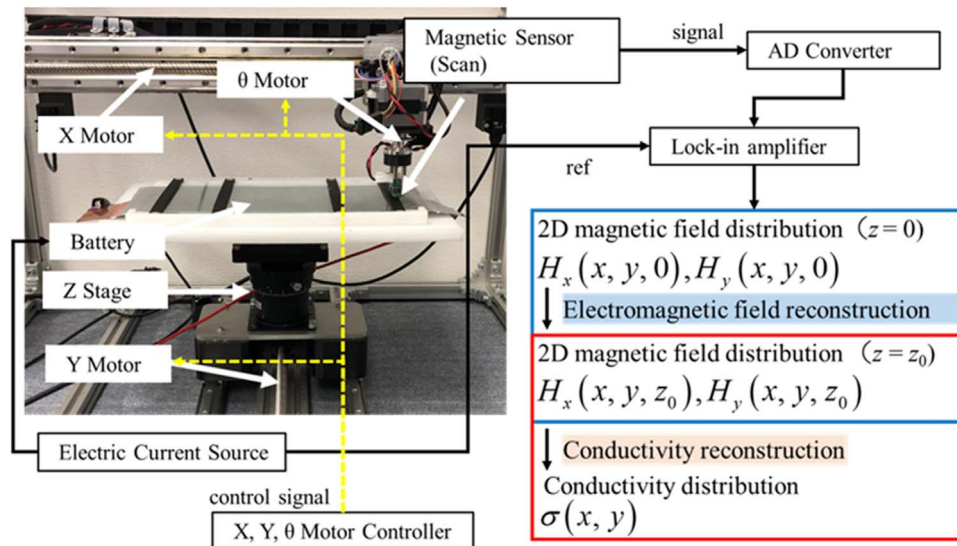


Fig. 2. (Color online) Magnetic imaging system and overview of the process to visualize the conductivity distribution in a lithium-ion battery.

carbonate (VC). The cycle test was performed at 15 °C. The battery was charged and discharged by DC. The charging current was 2250 mA (5 C), the control voltage was 4.2 V, and the stop condition was set at 45 mA (0.1 C). The discharging current was 450 mA (1 C) and the stop voltage was set at 2.5 V. The capacity of the battery before the cycle test was 469 mAh, and those after 100 and 200 cycles were 419 mAh and 252 mAh, respectively, with the progressive decrease in capacity upon repeated cycle tests. The capacity was measured at the test temperature of 25 °C. The battery was charged by constant-current/constant-voltage charging, and discharged by constant-current discharging. The charging/discharging conditions were 45 mA (0.1 C) for constant current charging, 4.2 V for constant voltage charging control voltage, 9 mA (0.02 C) for stop condition, 45 mA (0.1 C) for constant current discharge and 2.5 V for stop voltage. The magnetic field distribution was measured before the cycle test, after 100 cycles, and after 200 cycles. The magnetic field was measured by applying to the battery the AC (1 Hz, 240 mAp-p) superimposed with the DC voltage of 3.4 V. Using the non-destructive magnetic imaging system illustrated in Fig. 2, measuring magnetic field was performed over the area of 260 mm × 120 mm divided into 32 × 16 pixels, and one measurement time was 3.6 h per frame. By processing the difference between the magnetic field distributions before and after the cycles following Eq. (9), we visualized the changes in the conductivity distribution during the cycle test. This procedure makes it possible to visualize only the changes in conductivity inside the battery associated with cycle deterioration, and to neglect the initial current density distribution bias. Figures 3(a) and 3(b) show the results of the spatial distribution of H_x and H_y components of the magnetic field leaking from the lithium-ion battery before the cycle test. Figures 3(c) and 3(d) show the spatial

distribution of H_x and H_y after the cycle test (100 times), Figs. 3(e) and 3(f) show the difference between the spatial distributions of H_x and H_y on the battery surface before and after the 100 cycles. Figure 3(g) visualizes the conductivity distribution basing on the data in Figs. 3(e) and 3(f) calculated using Eq. (9). Furthermore, Figs. 3(h) and 3(i) show the spatial distribution of H_x and H_y before and after the 200 cycles, and Figs. 3(j) and 3(k) show the difference between the spatial distributions H_x and H_y on the battery surface before and after the 200 cycles. Moreover, Fig. 3(l) visualizes the conductivity distribution basing on the data in Figs. 3(j) and 3(k). Following Figs. 3(g) and 3(l), it is clear that the changes associated with the cycle test were most significant in the center of the battery, and the region of abnormal conductivity expands during the cycle tests. The spatial resolution of this system is determined by the size of the magnetic sensor and is 5 mm. The detection limit of the leakage current of a short circuit is determined by the detectability of the magnetic sensor, which is 27 μ A in the case of a point short circuit with a sensor-sample distance of 2 mm.

4. Conclusions

In this study, we visualized the spatial changes in the conductivity distribution inside a Li-ion battery due to cycle deterioration by measuring the magnetic field generated by the current flowing during its operation. In addition, we successfully identified the deteriorated part causing the battery capacity to decrease during the charging–discharging cycles. Furthermore, as this system provides a non-destructive analysis, the defective part size and shape can be tracked during the cycle tests. Thus, it was demonstrated that the developed system was efficient for visualizing the short circuits that occurred in lithium-ion batteries.

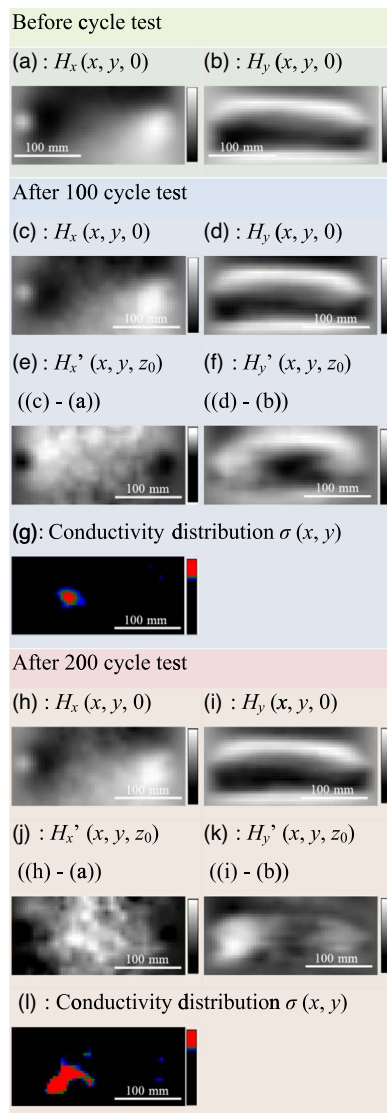


Fig. 3. (Color online) (a) Magnetic field distribution before cycle test [$H_x(x, y, 0)$] obtained by magnetic imaging system; (b) magnetic field distribution before cycle test [$H_y(x, y, 0)$]; (c) magnetic field distribution after 100 cycles [$H_x(x, y, 0)$]; (d) magnetic field distribution after 100 cycles [$H_y(x, y, 0)$]; (e) difference in magnetic field distribution [$H_x'(x, y, z_0)$] before and after 100 cycles by applying the magnetic field reconstruction method; (f) difference in magnetic field distribution [$H_y'(x, y, z_0)$] before and after 100 cycles by applying the magnetic field reconstruction method; (g) conductivity distribution [$\sigma(x, y)$] obtained from the data of the measurements in (e) and (f) using Eq. (9); (h) magnetic field distribution after 200 cycles [$H_x(x, y, 0)$]; (i) magnetic field distribution after 200 cycles (200 times) [$H_y(x, y, 0)$]; (j) difference in magnetic field distribution [$H_x'(x, y, z_0)$] before and after 200 cycles by applying the magnetic field reconstruction method; (k) difference in magnetic field distribution [$H_y'(x, y, z_0)$] before and after 200 cycles by applying the magnetic field reconstruction method; (l) conductivity distribution [$\sigma(x, y)$] obtained from the data of the measurements in (j) and (k) using Eq. (9).

Acknowledgments

This work was partially supported by NEDO (New Energy and Industrial Technology Development Organization).

- 1) K. J. Harry, D. T. Hallinan, D. Y. Parkinson, A. A. MacDowell, and N. P. Balsara, *Nat. Mater.* **13**, 69 (2014).
- 2) Z. Li, J. Huang, B. Yann Liaw, V. Metzler, and J. Zhang, *J. Power Sources* **254**, 168 (2014).
- 3) G. Bieker, M. Winter, and P. Bieker, *Phys. Chem. Chem. Phys.* **17**, 8670 (2015).
- 4) L. A. Selis and J. M. Seminario, *RSC Adv.* **8**, 255 (2018).
- 5) M. Arakawa, S. Tobishima, Y. Nemoto, M. Ichimura, and J. Yamaki, *J. Power Sources* **43**, 27 (1993).
- 6) C. Fringant, A. Tranhant, and R. Messina, *Electrochim. Acta* **40**, 513 (1995).
- 7) F. Orsini, A. Du Pasquier, B. Beaudouin, J. M. Tarascon, M. Trentin, N. Langenhuisen, E. De Beer, and P. Notten, *J. Power Sources* **76**, 19 (1998).
- 8) P. Arora, M. Doyle, and R. E. White, *J. Electrochem. Soc.* **146**, 3543 (1999).
- 9) X. Feng, Y. Pan, X. He, L. Wang, and M. Ouyang, *J. Energy Storage* **18**, 26 (2018).
- 10) L. Liu, X. Feng, M. Zhang, L. Lu, X. Han, X. He, and M. Ouyang, *Appl. Energy* **259**, 114143 (2020).
- 11) Y. Liu, P. Sun, H. Niu, X. Huang, and G. Rein, *Fire Saf. J.* **120**, 103081 (2021).
- 12) P. Sun, R. Bisschop, H. Niu, and X. Huang, *Fire Technol.* **56**, 1361 (2020).
- 13) C. Brissot, M. Rosso, J.-N. Chazalviel, P. Baudry, and S. Lascaud, *Electrochim. Acta* **43**, 1569 (1998).
- 14) C. Brissot, M. Rosso, J.-N. Chazalviel, and S. Lascaud, *J. Power Sources* **81**, 925 (1999).
- 15) K. Nishikawa, T. Mori, T. Nishida, Y. Fukunaka, and M. Rosso, *J. Electroanal. Chem.* **661**, 84 (2011).
- 16) S. Santhanagopalan, P. Ramadass, and J. Zhang, *J. Power Sources* **194**, 550 (2009).
- 17) J. Liu, M. Kunz, K. Chen, N. Tamura, and T. J. Richardson, *J. Phys. Chem. Lett.* **1**, 2120 (2010).
- 18) S. Imashuku, H. Taguchi, T. Kawamata, S. Fujieda, S. Kashiwakura, S. Suzuki, and K. Wagatsuma, *J. Power Sources* **399**, 186 (2018).
- 19) M. Katayama, K. Sumioka, R. Miyahara, H. Yamashige, H. Arai, Y. Uchimoto, K. Ohara, Y. Inada, and Z. Ogumi, *J. Power Sources* **269**, 994 (2014).
- 20) P. R. Shearing, L. E. Howard, P. S. Jørgensen, N. P. Brandon, and S. J. Harris, *Electrochem. Commun.* **12**, 374 (2010).
- 21) M. Ebner, F. Marone, M. Stamparoni, and V. Wood, *Science* **342**, 716 (2013).
- 22) G. Ouvrard, M. Zerrouki, P. Soudan, B. Lestriez, C. Masquelier, M. Morcrette, S. Hamelet, S. Belin, A. M. Flank, and F. Baudalet, *J. Power Sources* **229**, 16 (2013).
- 23) T. Nakamura, T. Watanabe, K. Amezuwa, H. Tanida, K. Ohara, Y. Uchimoto, and Z. Ogumi, *Solid State Ion.* **262**, 66 (2014).
- 24) T. Nakamura, T. Watanabe, Y. Kimura, K. Amezuwa, K. Nitta, H. Tanida, K. Ohara, Y. Uchimoto, and Z. Ogumi, *J. Phys. Chem. C* **121**, 2118 (2017).
- 25) D. Burow, K. Sergeeva, S. Calles, K. Schorb, A. Börger, C. Roth, and P. Heitjans, *J. Power Sources* **307**, 806 (2016).
- 26) P. Zhang, T. Yuan, Y. Pang, C. Peng, J. Yang, Z. F. Ma, and S. Zheng, *J. Electrochem. Soc.* **166**, A5489 (2019).
- 27) M. Kerlau, M. Marcinek, V. Srinivasan, and R. M. Kostecki, *Electrochim. Acta* **52**, 5422 (2007).
- 28) J. Nanda, J. Remillard, A. O'Neill, D. Bernardi, T. Ro, K. E. Nietering, J. Y. Go, and T. J. Miller, *Adv. Funct. Mater.* **21**, 3282 (2011).
- 29) Y. Mima, N. Oyabu, T. Inao, N. Kimura, and K. Kimura, *Proc. of IEEE CPMT Symp., 2013 (Japan)* Vol. **257**, 10.1541/ieejjournal.135.437.
- 30) K. Kimura, Y. Mima, and N. Kimura, *Subsurf. Img. Sci. Technol.* **1**, 16 (2017).
- 31) K. Mohri, *Mater. Sci. Eng. A* **185**, 141 (1994).